

Electrically driven Rabi dynamics of magnetic-field-induced corner states in a two-dimensional topological insulator

D. V. Khomitsky,^{1,*} E. A. Lavrukina,² D. P. Krasavin,¹ S. S. Krishtopenko,³ and F. Teppe^{3,†}

¹*National Research Lobachevsky State University of Nizhny Novgorod,
Department of Physics, 23 Gagarin Avenue, 603022 Nizhny Novgorod, Russia*

²*National Research Lobachevsky State University of Nizhny Novgorod,*

Research Physicotechnical Institute, 23 Gagarin Avenue, 603022 Nizhny Novgorod, Russia

³*Laboratoire Charles Coulomb (L2C), UMR 5221 CNRS-Université de Montpellier, F-34095 Montpellier, France*

(Dated: May 28, 2026)

We study coherent electric manipulation of magnetic-field-induced localized states at a double kink of a helical edge in a HgTe/CdHgTe quantum well. An in-plane magnetic field opens a gap in the one-dimensional edge spectrum, while changes in the edge orientation generate localized in-gap states at the kinks. We show that, for suitable geometry and magnetic-field direction, two such states form an effective lithographically defined two-level subsystem. Using an edge-state model that includes both the localized levels and the continuum states outside the magnetic-field-induced gap, we calculate the electric-dipole matrix elements and solve the time-dependent problem under resonant driving. The resulting dynamics exhibits Rabi oscillations with linear frequencies of 20–40 GHz for realistic parameters. We find that the continuum states provide a leakage channel whose strength is strongly controlled by the driving amplitude: reducing the electric field suppresses leakage below the percent level while preserving GHz-scale coherent oscillations. These results establish a route from magnetic-field-induced corner-state physics to electrically driven two-level dynamics in a realistic two-dimensional topological-insulator edge geometry.

I. INTRODUCTION

Two-dimensional (2D) topological insulators (TIs) realizing the quantum spin Hall phase are characterized by an insulating bulk gap and gapless one-dimensional (1D) helical edge states [1–4]. Their key transport signature is a quantized conductance at zero magnetic field, associated with current carried by counterpropagating spin-momentum-locked edge modes. HgTe/CdHgTe quantum wells (QWs) provided the first semiconductor platform in which the quantum spin Hall phase was both theoretically predicted [3] and subsequently observed experimentally at millikelvin temperatures [4]. Since then, the family of experimentally realized 2D TIs has expanded beyond HgTe-based systems. Quantized edge transport has been reported in monolayer WTe₂ up to temperatures of order 100 K [5], and, more recently, in inverted three-layer InAs/GaInSb/InAs QWs up to 60 K [6, 7]. These developments establish semiconductor QWs and related van der Waals systems as versatile platforms for studying and controlling helical edge states.

The development of boundary-state concepts in topological phases has led to the notion of higher-order topological insulators (HOTIs) [8–13]. In a conventional d -dimensional TI, topological states appear at $(d - 1)$ -dimensional boundaries. By contrast, an HOTI hosts boundary modes at higher codimension. In two dimensions, this corresponds to zero-dimensional (0D) states localized at the corners of the sample. Experimental sig-

natures of such corner states have been reported in artificial 2D systems realizing quadrupole topological phases, including mechanical and microwave metamaterials [14, 15], as well as in second-order photonic crystals [16]. In semiconductor heterostructures, a 2D HOTI phase has been theoretically proposed for double HgTe/CdHgTe QWs [17–21] and three-layer InAs/Ga(In)Sb QWs [22–26] with double band inversion [27].

The possibility of generating corner states in quantum spin Hall systems by an external magnetic field has attracted considerable attention. In several works it was argued that applying an in-plane magnetic field to a 2D TI may drive the system into a second-order topological phase with states localized at the sample corners [28–30]. From the edge-state perspective, the magnetic field gaps the 1D helical spectrum through the Zeeman coupling and produces an effective edge mass. This mass depends on both the crystallographic orientation of the edge and the direction of the magnetic field. Therefore, when the edge direction changes abruptly, for example at a lithographically defined kink, the corresponding mass term changes as well, and a localized in-gap state may appear at the kink. However, the mere presence of a discrete level inside the magnetic-field-induced edge gap is not sufficient to identify it as a HOTI mode protected by a stable bulk invariant. It was recently shown that, in realistic 2D TIs based on HgTe/CdHgTe and InAs/GaInSb/InAs QWs, such magnetic-field-induced corner states should in general be understood as bound states of the effective edge theory, controlled by the relative configuration of magnetic-field-induced edge mass vectors, rather than as topologically protected HOTI corner modes [31]. At the same time, the absence of topological protection in this strict sense does not preclude

* khomitsky@phys.unn.ru

† frederic.teppe@umontpellier.fr

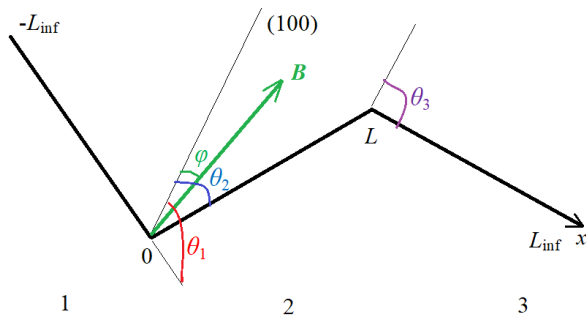


FIG. 1. Schematic of a HgTe/CdHgTe QW edge containing two lithographically defined kinks, which divide the edge into regions 1, 2, and 3. The orientations of the three edge segments are specified by the angles $\theta_{1,2,3}$ measured with respect to the crystallographic direction (100). The central segment lies along the x direction and extends from $x = 0$ to $x = L$. The in-plane magnetic field \mathbf{B} forms an angle ϕ with the (100) direction. The full edge is truncated at a length $L_{\text{inf}} \gg L$.

their spectral robustness against weak local perturbations, including short-range static disorder [32–34], as long as the corresponding levels remain isolated inside the edge gap. Together with the possibility of controlling their energy, localization length, and existence condition by the edge geometry and magnetic-field orientation, this makes magnetic-field-induced corner states a promising basis for tunable zero-dimensional levels in semiconductor heterostructures.

In the present work we go beyond the existence problem for a single magnetic-field-induced corner state and consider a 2D TI whose edge contains two lithographically defined kinks, as schematically shown in Fig. 1. The two corresponding in-gap states, localized inside the magnetic-field-induced gap of the 1D edge spectrum, can form an effective two-level subsystem. Unlike conventional electrostatically confined levels, this subsystem is defined by the edge geometry and by the magnetic-field-induced edge masses, and its parameters can be tuned by the kink separation and by the orientation of the in-plane magnetic field. This provides a simple setting for studying coherent electric-field-driven dynamics between two localized edge-state levels.

Related ideas of electrically controlled dynamics of localized states at the edge of a TI have been considered previously for models with one [35] and two [36] quantum dots defined by magnetic barriers. From the perspective of possible qubit-oriented architectures, the key requirement is the availability of two isolated and controllable discrete levels between which resonant transitions can be driven with weak leakage into continuum states. A conceptually related proposal was also put forward for a HgTe/CdHgTe QW patterned by a periodic array of holes, where a pair of discrete levels appears inside the minigap of the superlattice spectrum [37]. In contrast to such a superlattice-based realization, the system considered below forms the two localized levels directly at lithographically defined kinks of a single edge. Their

properties are therefore controlled by the edge geometry and by the orientation of the in-plane magnetic field, rather than by an extended periodic modulation.

The main goal of this work is to go beyond the spectral problem of forming magnetic-field-induced corner states and to analyze their driven dynamics in the presence of continuum edge states. We consider a double-kink edge geometry in which two localized in-gap states form inside the magnetic-field-induced edge gap. This geometry does not merely provide a pair of discrete levels; it also creates a controlled setting in which coherent resonant transfer, electric-dipole coupling, and leakage into the continuum can be treated within the same effective edge-state framework. We determine the parameter range in which two localized states exist, calculate their localization properties and dipole matrix elements, and then solve the time-dependent problem under resonant electric driving.

The resulting dynamics is governed by a competition between coherent population transfer and continuum-induced leakage. A stronger electric field increases the Rabi frequency and shortens the manipulation time, but also enhances population loss from the effective two-level subsystem [35]. A weaker field suppresses leakage at the cost of a longer Rabi period. The double-kink geometry therefore provides a concrete platform for studying the trade-off between fast electric control and the preservation of a two-level regime. The paper is organized as follows. In Sec. II we formulate the model and analyze the formation of two discrete localized levels. In Sec. III we construct the continuum edge states and evaluate the relevant transition matrix elements. In Sec. IV we study the resonant dynamics, including Rabi oscillations and leakage into the continuum. Finally, Sec. V summarizes the main results.

II. HAMILTONIAN AND SPECTRUM OF LOCALIZED STATES

Let us consider a 2D TI based on a HgTe/CdHgTe QW whose edge contains two kinks, as schematically shown in Fig. 1. The coordinate x is chosen along the bent edge such that the first kink is located at $x = 0$ and the second one at $x = L$. The edge segment between the two kinks defines region 2, whereas the two extended outer segments correspond to regions 1 and 3. The crystallographic orientation of the edge is described by the angle $\theta = \theta(x)$ measured with respect to the (100) direction. In the geometry considered below, $\theta(x)$ is a piecewise constant function taking the values θ_1 , θ_2 , and θ_3 in regions 1, 2, and 3, respectively. A static magnetic field \mathbf{B} is applied in the plane of the QW and forms an angle ϕ with the (100) direction. Therefore, the change of edge orientation at $x = 0$ and $x = L$ leads to a change of the magnetic-field-induced mass terms in the effective edge Hamiltonian, which may produce localized states at the two kinks. The outer edge segments are assumed to be sufficiently long, so that the total computational length

L_{inf} satisfies $L_{\text{inf}} \gg L$ and is used below for the normalization of wave functions.

A. Low-energy model for the edge states

To describe the low-energy edge states of a 2D TI in a static magnetic field, we use the effective edge Hamiltonian [31]

$$H_0 = \hbar v_F k_x \sigma_z + M_x(x) \sigma_x + M_y(x) \sigma_y. \quad (1)$$

Here the first term describes the gapless helical edge states of the BHZ model [3], while the second and third terms are magnetic-field-induced mass terms generated by the Zeeman coupling to an in-plane magnetic field. The Pauli matrices σ_i act in the space of the two counter-propagating edge modes. For the geometry considered in Fig. 1, the magnetic field lies in the QW plane and forms an angle ϕ with the crystallographic direction (100). The mass terms are then written as

$$M_x(x) = \frac{E_Z}{2} [g_+ \cos(\theta(x) - \phi) + g_- \cos(3\theta(x) + \phi)],$$

$$M_y(x) = \frac{E_Z}{2} [g_+ \sin(\theta(x) - \phi) + g_- \sin(3\theta(x) + \phi)], \quad (2)$$

where $E_Z = g_1 \mu_B B / 2$ is the Zeeman energy scale and $g_{\pm} = 1 \pm g_2 / g_1$. The parameters g_1 and g_2 are combinations of the components of the edge-state g -factor tensor. Since $\theta(x)$ is piecewise constant, the mass vector (M_x, M_y) is also piecewise constant and changes abruptly at the two kinks.

Neglecting the contributions related to the lack of inversion symmetry in the bulk unit cell of HgTe and CdHgTe, namely bulk inversion asymmetry (BIA) [38], as well as possible interface inversion asymmetry (IIA) of HgTe/CdHgTe heterointerfaces [39], the parameters of the edge Hamiltonian take a simple form. This approximation is justified for realistic HgTe/CdHgTe QWs, where the BIA and IIA terms are small [40, 41]. In this case one obtains [31]

$$\hbar v_F = \mathbb{A} \sqrt{1 - \eta^2}, \quad (3)$$

and

$$\begin{aligned} g_1 &= g_e^{(\parallel)} \frac{1 - \eta}{2} + g_h^{(\parallel)} \frac{1 + \eta}{2}, \\ g_2 &= g_e^{(\parallel)} \frac{1 - \eta}{2} - g_h^{(\parallel)} \frac{1 + \eta}{2}, \end{aligned} \quad (4)$$

where $\eta = \mathbb{D} / \mathbb{B}$. Here $g_e^{(\parallel)}$ and $g_h^{(\parallel)}$ are the in-plane g factors of the $E1$ and $H1$ subbands, respectively. They originate from the contributions of the bulk Γ_6 , Γ_8 , and Γ_7 bands [42]. The parameters \mathbb{A} , \mathbb{B} , \mathbb{D} , $g_e^{(\parallel)}$, and $g_h^{(\parallel)}$ depend on the QW width and on the Cd content in the CdHgTe barriers. In the numerical calculations below

we use $\mathbb{A} = 365 \text{ meV}\cdot\text{nm}$, $\mathbb{B} = -768 \text{ meV}\cdot\text{nm}^2$, $\mathbb{D} = -593 \text{ meV}\cdot\text{nm}^2$, $g_e^{(\parallel)} = 27$, and $g_h^{(\parallel)} = -1.2$. These values are characteristic of a 7 nm-wide HgTe/Cd_{0.7}Hg_{0.3}Te QW grown on a (001)-oriented CdTe buffer [43]. For this prototype QW, Eqs. (4) yield

$$g_1 = 2.012, \quad g_2 = 4.139. \quad (5)$$

The eigenfunctions of Hamiltonian (1) are sought in the form of two-component spinors

$$\psi_x = \begin{pmatrix} a \\ b \end{pmatrix} e^{\lambda x}, \quad (6)$$

where the parameter λ can be either purely imaginary or real. In the former case, the solutions describe propagating edge states with plane-wave factors $\exp(\pm i k_x x)$. For a given region $n = 1, 2, 3$, where the edge orientation is fixed and the mass terms are constant, Hamiltonian (1) gives the continuum spectrum schematically shown in Fig. 2,

$$\varepsilon_{1,2}(k_x(n)) = \pm \sqrt{k_x(n)^2 + |M_n|^2}. \quad (7)$$

Here $\varepsilon_{1,2}(k_x(n)) = E_{1,2}(k_x(n)) / (\hbar v_F)$ is the energy rescaled by $\hbar v_F$, and the index n labels the three spatial regions shown in Fig. 1. Thus, a state with the same rescaled energy ε generally corresponds to different longitudinal wave vectors $k_x(n)$ in different regions.

The in-plane magnetic field opens a common gap $2\Delta_B$ in the edge-state spectrum with

$$\Delta_B = \min_{n=1,2,3} |\hbar v_F M_n|, \quad (8)$$

where

$$|M_n|^2 = \frac{(M_x(n))^2 + (M_y(n))^2}{(\hbar v_F)^2}. \quad (9)$$

The quantities $M_{x,y}(n)$ are obtained from Eq. (2) by setting $\theta = \theta_n$ in the corresponding region. The discrete localized levels considered below lie inside this common magnetic-field-induced gap. For energies outside this interval, at least one of the three edge regions supports propagating continuum states. The corresponding propagating solutions described by the spectrum (7) will be considered in the next section. Here we focus on localized states, for which the parameter λ in Eq. (6) is real and the wave functions decay away from the edge kinks, as illustrated in Fig. 2.

The boundary conditions for localized states are given by the continuity of the wave function at the two kinks, $x = 0$ and $x = L$, together with the decay of the wave function at infinity:

$$\begin{cases} \Psi(x \rightarrow \pm\infty) = 0, \\ \Psi(x+0) = \Psi(x-0), \quad \Psi(L+0) = \Psi(L-0). \end{cases} \quad (10)$$

These conditions are satisfied by the following piecewise-defined solutions. In region 1, for $x < 0$, the wave function is written as

$$\Psi_1(x) = A \left(\frac{1}{\sqrt{|M_1|^2 - \varepsilon^2} - i\varepsilon} \right) e^{\sqrt{|M_1|^2 - \varepsilon^2} x}, \quad (11)$$

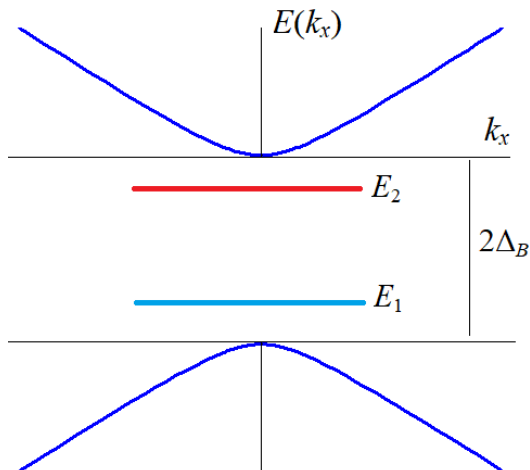


FIG. 2. Schematic of the spectrum consisting of two continuum branches described by Eq. (7). The magnetic field opens a common gap $2\Delta_B$ in the edge spectrum, with $\Delta_B = \min_n \sqrt{M_x^2(n) + M_y^2(n)}$. For the double-kink geometry shown in Fig. 1, two discrete levels $E_{1,2}$ may appear inside this gap for suitable parameters. The corresponding wave functions are localized at the kinks of the edge.

where

$$M_{\pm n} = \frac{M_x(n) \pm iM_y(n)}{\hbar v_F}. \quad (12)$$

The coefficient A is determined from the boundary conditions (10).

In region 2, for $0 < x < L$, the localized-state solution contains both increasing and decreasing exponential components,

$$\begin{aligned} \Psi_2(x) = & B_1 \left(\frac{1}{\sqrt{|M_2|^2 - \varepsilon^2} - i\varepsilon} \right) e^{\sqrt{|M_2|^2 - \varepsilon^2} x} \\ & + B_2 \left(\frac{1}{-\sqrt{|M_2|^2 - \varepsilon^2} - i\varepsilon} \right) e^{-\sqrt{|M_2|^2 - \varepsilon^2} x}. \end{aligned} \quad (13)$$

In region 3, for $x > L$, the decaying solution has the form

$$\Psi_3(x) = C \left(\frac{1}{-\sqrt{|M_3|^2 - \varepsilon^2} - i\varepsilon} \right) e^{-\sqrt{|M_3|^2 - \varepsilon^2} x}. \quad (14)$$

The coefficients A , B_1 , B_2 , and C are found from the boundary conditions (10). Substituting Eqs. (11)–(14) into these conditions gives a homogeneous system of linear equations for the four coefficients. After solving this system, the resulting wave functions are normalized on the full x axis. Nontrivial solutions exist only at rescaled energies ε_i satisfying the characteristic equation

$$\Delta(\varepsilon_i) = 0, \quad (15)$$

where Δ is the determinant of the coefficient matrix. Equation (15) is solved numerically for different sets of

parameters $\theta_{1,2,3}$, ϕ , and L . In the following subsection, we identify the regions of this parameter space where Eq. (15) has two rescaled-energy solutions $\varepsilon_{1,2}$ corresponding to two localized states that can be resonantly coupled by a time-periodic electric field.

B. Numerical results for localized states

The analysis of the characteristic equation (15) shows that the broadest parameter region in which two discrete levels exist inside the gap shown in Fig. 2 is obtained for the symmetric choice $\theta_3 = \theta_1$ in Fig. 1. For definiteness, we set $\theta_2 = 0$ in the following and, at fixed magnetic-field amplitude, perform the search for solutions of Eq. (15) in the (θ_1, ϕ) parameter plane.

In the numerical calculations we choose $E_Z = 150 \mu\text{eV}$. With the edge-state g factors given in Eq. (5), this value corresponds to an in-plane magnetic field $B = 1.6 \text{ T}$, which is readily accessible in experiments on 2D TIs. We consider a structure with the length of the central edge segment $L = 250 \text{ nm}$. This corresponds to a mesoscopic sample size compatible with realistic lithographic fabrication constraints.

An example of the calculated discrete spectrum in the (θ_1, ϕ) parameter plane is shown in Fig. 3. Panel (a) presents the energies of the two discrete levels in units of E_Z . The uniform background regions at the top and bottom of the panel correspond to parameter values for which a pair of localized levels is not formed. The black circles mark the levels $E_1 = -1.342 E_Z$ and $E_2 = 1.342 E_Z$, obtained for $\theta_1 = \theta_3 = 2\pi/3$ and $\phi = \pi/2$. This pair of levels is used in most of the calculations below. The choice of these parameters is also motivated by the spin properties of the corresponding states. Panels (b) and (c) of Fig. 3 show the x component of spin, S_x , in units of $\hbar/2$, for the lower and upper levels in panel (a). For the selected pair of states, the values of S_x are nearly equal in magnitude and opposite in sign. This property is useful for associating the two localized levels with opposite projections of spin along the x direction in possible applications of the structure as a controllable two-level subsystem.

For the pair of levels chosen in Fig. 3, the absolute value of the dipole matrix element

$$X_{12} = \langle \Psi_1 | x | \Psi_2 \rangle \quad (16)$$

is sufficiently large for efficient electric driving. Here the matrix element is calculated using the wave functions of the two discrete states marked in Fig. 3(a). Figure 4(a) shows the probability-density distributions for the states Ψ_1 and Ψ_2 corresponding to the lower and upper discrete levels in Figs. 2 and 3. Figure 4(b) presents the absolute value of the dipole matrix element (16) over the full parameter plane $(\theta_1 = \theta_3, \phi)$.

As seen from Fig. 4(a), the lower and upper discrete states are localized predominantly near the left kink at $x = 0$ and the right kink at $x = L$, respectively. For the

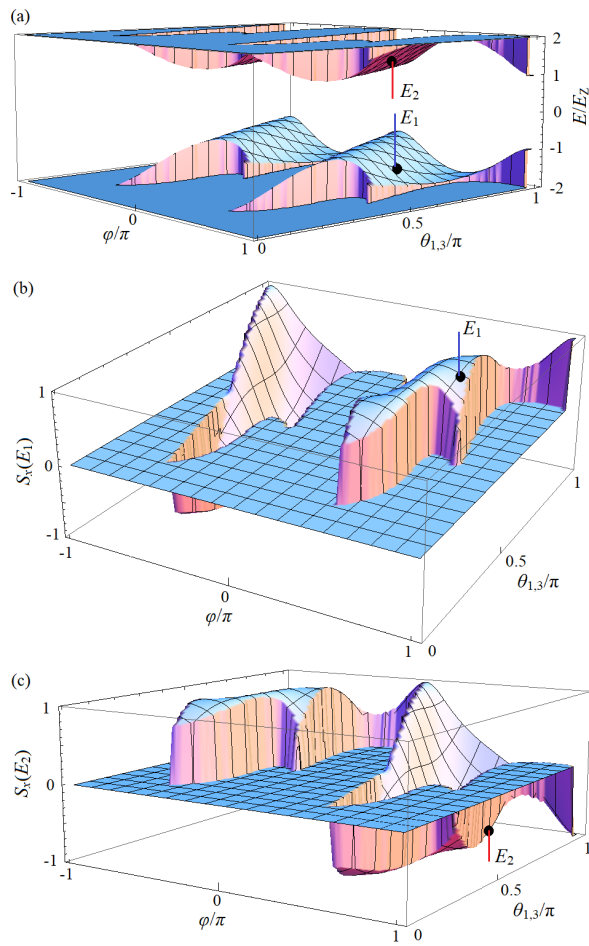


FIG. 3. (a) Spectrum of the two discrete levels $E_{1,2}$ shown schematically in Fig. 2 as a function of the angles $\theta_1 = \theta_3$ and ϕ defined in Fig. 1. The other parameters are $\theta_2 = 0$, $L = 250$ nm, and $E_Z = 150$ μ eV. The uniform background regions at the top and bottom correspond to the absence of a pair of localized levels. The selected levels $E_{1,2} = \mp 1.342 E_Z$ at $\theta_1 = \theta_3 = 2\pi/3$ and $\phi = \pi/2$ are marked by black circles. (b), (c) Distributions of the x component of spin for the lower (b) and upper (c) levels shown in panel (a). For the selected pair of levels, the x -spin projections have opposite signs and nearly equal magnitudes.

selected pair of levels, Fig. 4(b) gives $|X_{12}| = 885$ nm. This large dipole matrix element enables high-frequency resonant transitions driven by an external electric field, as discussed below.

III. CONTINUUM STATES AND TRANSITION MATRIX ELEMENTS

Although the main focus of this work is on the states localized at the kinks of the edge in Fig. 1, the continuum states outside the magnetic-field-induced gap $2\Delta_B$ given by Eq. (8) and shown in Fig. 2 should also be taken into account in the dynamical problem. Under a

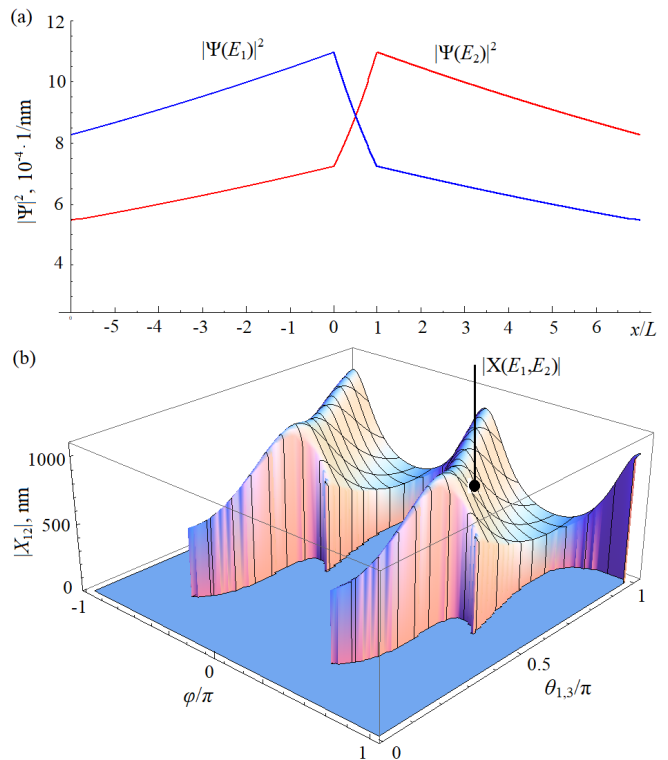


FIG. 4. (a) Probability-density distributions $|\Psi|^2$ for the levels $E_{1,2}$ marked in Fig. 3. The two states are localized near the left and right ends of the central segment $0 < x < L$ in Fig. 1. (b) Absolute value of the dipole matrix element (16) as a function of the angles $\theta_1 = \theta_3$ and ϕ . The marked value $|X_{12}| = 885$ nm corresponds to the selected pair of discrete levels whose probability-density distributions are shown in panel (a).

time-periodic electric field, these states can be coupled to the localized levels and thus provide a leakage channel out of the effective two-level subsystem. In the double-kink geometry, propagating continuum states are partially reflected and transmitted at the two kinks, $x = 0$ and $x = L$. Therefore, their wave functions cannot be represented by a single expression of the form (6) over the entire edge. Instead, they are constructed piecewise in regions 1, 2, and 3, in analogy with the localized states (11)–(14), but with purely imaginary exponents. For a fixed energy in the spectrum of Eq. (7), there are two families of propagating states: states $\Psi^{(R)}$ incident from the left and propagating from left to right, and states $\Psi^{(L)}$ incident from the right and propagating from right to left. Both families are constructed for energies

$$|E| = \hbar v_F |\varepsilon| > \Delta_B. \quad (17)$$

Let us first consider the states $\Psi^{(R)}$ corresponding to a wave incident from the left. In region 1 of Fig. 1, for $x < 0$, the wave function has the form

$$\Psi_1^{(R)}(x) = \begin{pmatrix} 1 \\ \alpha_{+1} \end{pmatrix} e^{ik_1 x} + A_{-1} \begin{pmatrix} 1 \\ \alpha_{-1} \end{pmatrix} e^{-ik_1 x}. \quad (18)$$

The first term in Eq. (18) describes the incident wave with unit amplitude, while the second term describes the wave reflected from the double-kink region. Here we introduce

$$\alpha_{\pm n} = \frac{\varepsilon \mp \sqrt{\varepsilon^2 - |M_n|^2}}{M_{-n}}, \quad k_n = \sqrt{\varepsilon^2 - |M_n|^2}, \quad (19)$$

where M_n and $M_{\pm n}$ are defined in Eqs. (9) and (12), respectively.

In region 2, for $0 < x < L$, the wave function contains two components propagating in opposite directions,

$$\Psi_2^{(R)}(x) = A_{+2} \begin{pmatrix} 1 \\ \alpha_{+2} \end{pmatrix} e^{ik_2x} + A_{-2} \begin{pmatrix} 1 \\ \alpha_{-2} \end{pmatrix} e^{-ik_2x}. \quad (20)$$

In region 3, for $x > L$, only the transmitted right-moving wave remains,

$$\Psi_3^{(R)}(x) = A_{+3} \begin{pmatrix} 1 \\ \alpha_{+3} \end{pmatrix} e^{ik_3x}. \quad (21)$$

The coefficients A_{-1} , $A_{\pm 2}$, and A_{+3} are determined from the continuity of the wave function at $x = 0$ and $x = L$, i.e., from the second and third conditions in Eq. (10). Substitution of Eqs. (18)–(21) gives a system of four inhomogeneous linear equations, where the inhomogeneous term originates from the incident wave of unit amplitude in Eq. (18). This system has a solution for any incident-wave energy satisfying Eq. (17). After the coefficients are found, the continuum wave functions are normalized to unity on a large but finite interval of length of order L_{inf} , with $L_{\text{inf}} \gg L$.

The second family of continuum states, $\Psi^{(L)}$, corresponds to waves incident from the right and propagating along the edge from right to left. These solutions are constructed in the same way as the states $\Psi^{(R)}$. The difference is that the incident wave with unit amplitude is proportional to e^{-ik_3x} and enters the solution in region 3, whereas in region 1 only the transmitted left-moving wave proportional to e^{-ik_1x} remains. The corresponding coefficients are again obtained from the continuity conditions at $x = 0$ and $x = L$, and the normalization is performed in the same way. In the dynamical calculations below, continuum states of both families, $\Psi^{(R)}$ and $\Psi^{(L)}$, are included.

For the numerical simulations of the dynamics discussed in the next section, the continuum states are discretized in energy. In the construction of the continuum wave functions, it is convenient to use the rescaled energy $\varepsilon = E/(\hbar v_F)$, which has the dimension of inverse length. However, the energy window used in the dynamical calculations is specified in terms of the physical energy E . Our calculations show that it is sufficient to include continuum states with physical energies in the interval $|E| < n_b \Delta_B$, where $n_b \sim 200$. Following our previous treatment of continuum-assisted dynamics for a quantum dot at the edge of a TI [35], we introduce a uniform discretization of this energy interval with the

step

$$\delta E = \frac{n_b \Delta_B}{N}, \quad (22)$$

where $N \sim 1000$. This discretization provides an adequate description of population leakage from the two-level subsystem into the continuum, caused by nonzero dipole matrix elements

$$X_{nE} = \langle \Psi_n | x | \Psi_E^{(R,L)} \rangle. \quad (23)$$

Here Ψ_n with $n = 1, 2$ denotes one of the localized states considered in the previous section, while $\Psi_E^{(R,L)}$ is a continuum state of either family with physical energy $E = \hbar v_F \varepsilon$.

In practice, the continuum states that contribute appreciably to the dynamics occupy a much narrower energy range than the full interval $|E| < n_b \Delta_B$. This is illustrated in Fig. 5, which shows the absolute values of the matrix elements (23) as functions of the physical energy E of the continuum states for transitions from the lower and upper discrete levels $E_{1,2}$ to the states of the family $\Psi^{(L)}$. Figure 5(a) corresponds to transitions into the lower continuum branch, $-n_b \Delta_B < E < -\Delta_B$, whereas Fig. 5(b) shows transitions into the upper continuum branch, $\Delta_B < E < n_b \Delta_B$. For the second family of continuum states, $\Psi^{(R)}$, the energy dependence of the matrix elements has a similar form.

As seen from Fig. 5, the matrix elements for transitions into the lower and upper continuum branches exhibit similar energy dependences and rapidly decrease away from the edges of the magnetic-field-induced gap. Only a part of the chosen energy window gives an appreciable contribution. The largest matrix elements occur near the continuum threshold; for the parameters considered here, the relevant transitions involve continuum states within several meV from the gap edges. Nevertheless, in the dynamical calculations below we retain all continuum states with physical energies in the intervals $[-n_b \Delta_B, -\Delta_B]$ and $[\Delta_B, n_b \Delta_B]$. For $n_b = 200$, this corresponds to an energy window of the order of $[-30, 30]$ meV and to approximately 2000 continuum states included in the calculation.

Extending this energy window further is not useful within the present low-energy edge-state model. At higher energies, the edge-state spectrum starts to overlap with bulk 2D states of the HgTe/CdHgTe QW, against which the edge contribution is no longer well separated [43]. The bulk 2D states in the considered QW lie outside a sufficiently large energy gap that contains the edge-state spectrum (7). Moreover, the rapid decrease of the matrix elements (23) in Fig. 5 suggests that transitions to even more distant bulk states should have small amplitudes. Such states are therefore not included in the approximation used below.

We note that the continuum-state model described above is not unique. In our previous studies of population leakage into the continuum from discrete donor

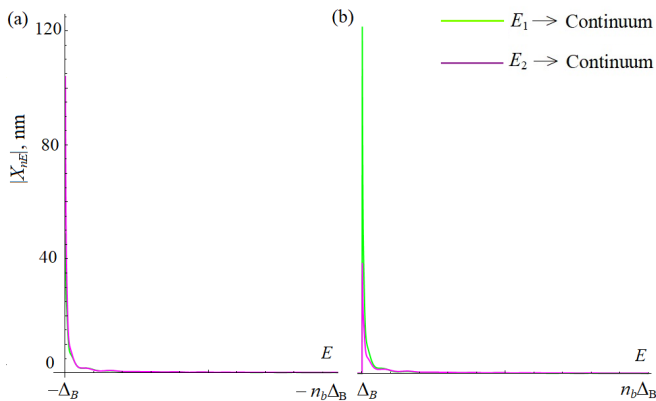


FIG. 5. Absolute value of the matrix element (23) for transitions into continuum states of the family $\Psi^{(L)}$: (a) lower continuum branch, $-n_b\Delta_B < E < -\Delta_B$, and (b) upper continuum branch, $\Delta_B < E < n_b\Delta_B$, with $n_b = 200$. Each panel shows transitions from the lower discrete level E_1 and from the upper discrete level E_2 .

levels [44] and from a multilevel quantum dot [45] in an InSb-based nanowire, the continuum was represented by a large number of closely spaced discrete levels. Each such level corresponded to a state localized in a large interval $[-L_{\text{inf}}, L_{\text{inf}}]$ with distant infinitely high walls. An analogous continuum model can also be constructed for the present system described by Hamiltonian (1). Our calculations show that this alternative approach gives results for the time evolution and characteristic leakage times that are close to those obtained with the two-family propagating-state model $\Psi^{(R,L)}$ introduced in this section. This robustness with respect to the continuum representation supports the reliability of the leakage description used here. In the following calculations of the dynamics in a periodic electric field, we use the continuum-state model constructed in this section.

IV. RESONANT DYNAMICS IN AN ELECTRIC FIELD

We now turn to the central dynamical problem of this work: resonant electric manipulation of the two magnetic-field-induced localized states in the presence of continuum edge states. The electric-field frequency is chosen to be resonant with the energy separation between the discrete levels $E_{1,2}$ shown in Fig. 2. The purpose of this analysis is to determine whether these two localized levels can operate as a controllable two-level subsystem once their coupling to continuum states outside the magnetic-field-induced gap is included explicitly. The electric field is treated in the quasistatic approximation through the scalar potential [35]

$$V(x, t) = -Fx \sin \omega t. \quad (24)$$

Here the electron charge is absorbed into F , so that F has the units of energy per length; below it is measured

in $\mu\text{eV}/\text{nm}$. We choose the resonant frequency corresponding to the transition energy between the two discrete levels, $\hbar\omega = E_2 - E_1 = 0.398$ meV, which gives the linear frequency $f = 96.4$ GHz. This frequency range is accessible with modern microwave and millimeter-wave techniques.

The solution of the time-dependent Schrödinger equation with the Hamiltonian $H_0 + V(x, t)$, where H_0 is defined in Eq. (1), is expanded over the stationary eigenstates $\Psi_n(x)$ as

$$\Psi(x, t) = \sum_n C_n(t) e^{-iE_n t/\hbar} \Psi_n(x). \quad (25)$$

This basis includes both the two localized states of the discrete spectrum discussed in Sec. II and the continuum states constructed in Sec. III. The expansion coefficients $C_n(t)$ obey the system of ordinary differential equations

$$\frac{dC_n}{dt} = i \frac{F}{\hbar} \sin \omega t \sum_l C_l(t) X_{nl} e^{-i(E_l - E_n)t/\hbar}. \quad (26)$$

The dynamics is governed by the dipole matrix elements of the coordinate operator, X_{nl} , introduced above in Eqs. (16) and (23). As the initial condition, we take the system to be fully populated on the lower discrete level E_1 .

The inclusion of continuum states is essential even when the harmonic electric field is tuned resonantly to the transition between the localized levels E_1 and E_2 . The coordinate operator couples the two localized states not only to each other but also to extended edge states outside the magnetic-field-induced gap. Therefore, the applicability of the two-level description is controlled by the competition between coherent resonant transfer and continuum-induced population loss. The field amplitude F controls both processes: increasing F enhances the Rabi frequency and shortens the manipulation time, while simultaneously increasing the leakage into the continuum [35]. Conversely, reducing F suppresses leakage but slows down the Rabi oscillations. Thus, the relevant figure of merit is not the Rabi frequency alone, but the relation between the Rabi period and the characteristic leakage time. The numerical analysis below is aimed at identifying an operating regime in which the Rabi oscillations remain fast, while the leakage stays weak over several oscillation periods.

We start with the field amplitude $F = 0.1 \mu\text{eV}/\text{nm}$. On the length scale of order $10L = 2.5 \mu\text{m}$, corresponding to the localization region of the states in Fig. 4(a), this amplitude produces a potential drop of about 0.25 meV. This value is smaller than the level spacing $E_2 - E_1$, but is already large enough for the coupling between the localized levels and the continuum states to be relevant. Therefore, the expansion (25) is performed in an extended basis including both the two discrete levels and the discretized continuum states.

An example of the calculated dynamics for $F = 0.1 \mu\text{eV}/\text{nm}$ is shown in Fig. 6. Panel (a) presents the

populations of the two discrete levels, $P_{1,2}(t) = |C_{1,2}(t)|^2$, together with the leakage probability into the continuum,

$$P_{\text{leak}} = 1 - |C_1|^2 - |C_2|^2. \quad (27)$$

The populations P_1 and P_2 exhibit Rabi oscillations with the linear frequency

$$f_R = 40 \text{ GHz}. \quad (28)$$

This value corresponds to characteristic manipulation times on the scale of several tens of picoseconds. At this stage, the coherent description should therefore be viewed as a first estimate of fast resonant dynamics. The actual applicability of such a two-level subsystem to qubit-oriented architectures requires a separate analysis of spin relaxation and decoherence mechanisms, which in HgTe/CdHgTe structures may depend sensitively on the transport regime and sample parameters [46, 47]. We also note that the localization region of the states remains mesoscopic and smaller than the characteristic localization length of magnetic-field-induced edge states estimated within the model of Ref. [48]. This supports the use of the effective edge-state description for the geometry considered here.

The leakage into the continuum, quantified by Eq. (27), increases on average over the time interval shown in Fig. 6(a). For applications relying on a well-defined two-level subsystem, this leakage should be minimized, and a value $P_{\text{leak}} \sim 0.05$ is already appreciable. Thus, the Rabi frequency in Eq. (28) obtained for $F = 0.1 \mu\text{eV}/\text{nm}$ is close to the upper practical limit set by the requirement of weak leakage. At the same time, the large value of f_R leaves room for reducing the field amplitude: as F is decreased, the Rabi frequency is expected to decrease approximately linearly, whereas the leakage into the continuum is suppressed much more strongly. This result shows that the field amplitude $F = 0.1 \mu\text{eV}/\text{nm}$ already approaches the upper useful range for the present two-level subsystem. The coherent oscillations are very fast, but the continuum channel becomes visible on the same time scale as the driven population transfer. Therefore, the main question is whether one can reduce the leakage substantially without slowing the Rabi dynamics to impractically long times. This motivates the comparison with weaker driving fields discussed below.

Let us now consider the expectation values of physical observables for the state, described by $\Psi(x, t)$ in Eq. (25). Figure 6(b) shows the time dependence of the mean coordinate $\langle X(t) \rangle$. It oscillates with the same frequency as the populations in Fig. 6(a), reflecting transitions between states localized predominantly near the left and right edge kinks. Similar Rabi-frequency oscillations are observed in the expectation value of the spin projection $\langle S_x(t) \rangle$, shown in Fig. 6(c). The state of the two-level subsystem can therefore be characterized either by its spatial localization or by the x component of spin. The other spin components, $\langle S_y(t) \rangle$ and $\langle S_z(t) \rangle$, also oscillate but contain faster components, which can be suppressed by time averaging of the signal.

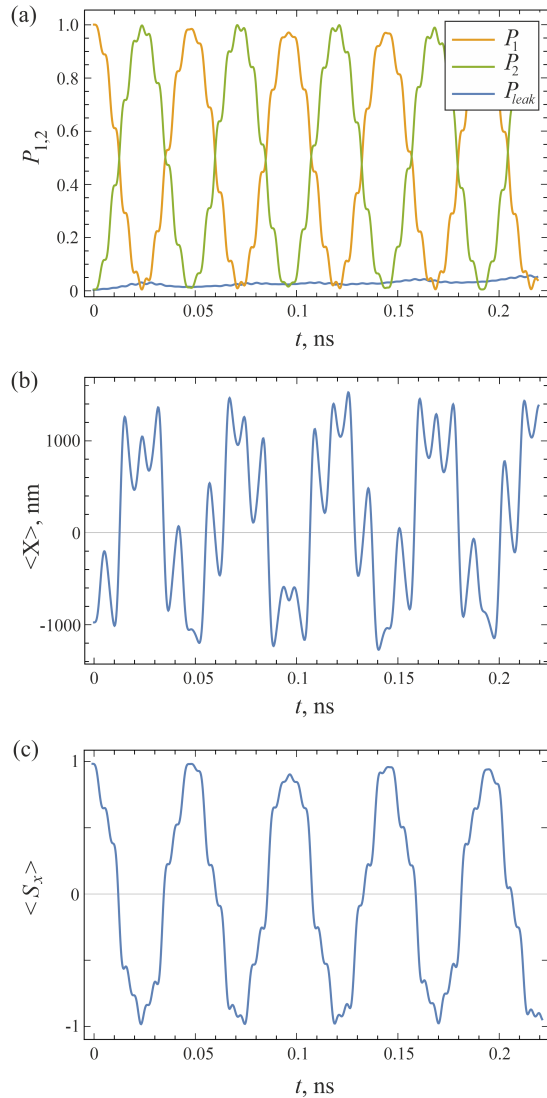


FIG. 6. Example of the dynamics for the field amplitude $F = 0.1 \mu\text{eV}/\text{nm}$. (a) Populations of the discrete levels, $P_{1,2}(t) = |C_{1,2}(t)|^2$, and leakage into the continuum, $P_{\text{leak}} = 1 - |C_1|^2 - |C_2|^2$. The dynamics shows Rabi oscillations with the linear frequency $f_R = 40 \text{ GHz}$ and leakage $P_{\text{leak}} \sim 0.05$ over a time interval of about 0.02 ns. (b,c) Time evolution of the expectation values $\langle X(t) \rangle$ and $\langle S_x(t) \rangle$. Both quantities follow the population oscillations in panel (a) and can be used to characterize the state of the two-level subsystem.

When the field amplitude is reduced from 0.1 to $0.05 \mu\text{eV}/\text{nm}$, the leakage rate decreases by more than one order of magnitude.

The effect of reducing the field amplitude is shown in Fig. 7, where the same quantities are plotted for $F = 0.05 \mu\text{eV}/\text{nm}$. As seen from Fig. 7(a), the Rabi frequency is reduced approximately by a factor of two and becomes $f_R = 20 \text{ GHz}$. The same characteristic frequency appears in the oscillations of $\langle X(t) \rangle$ and $\langle S_x(t) \rangle$ in panels (b) and (c). At the same time, the leakage into the continuum,

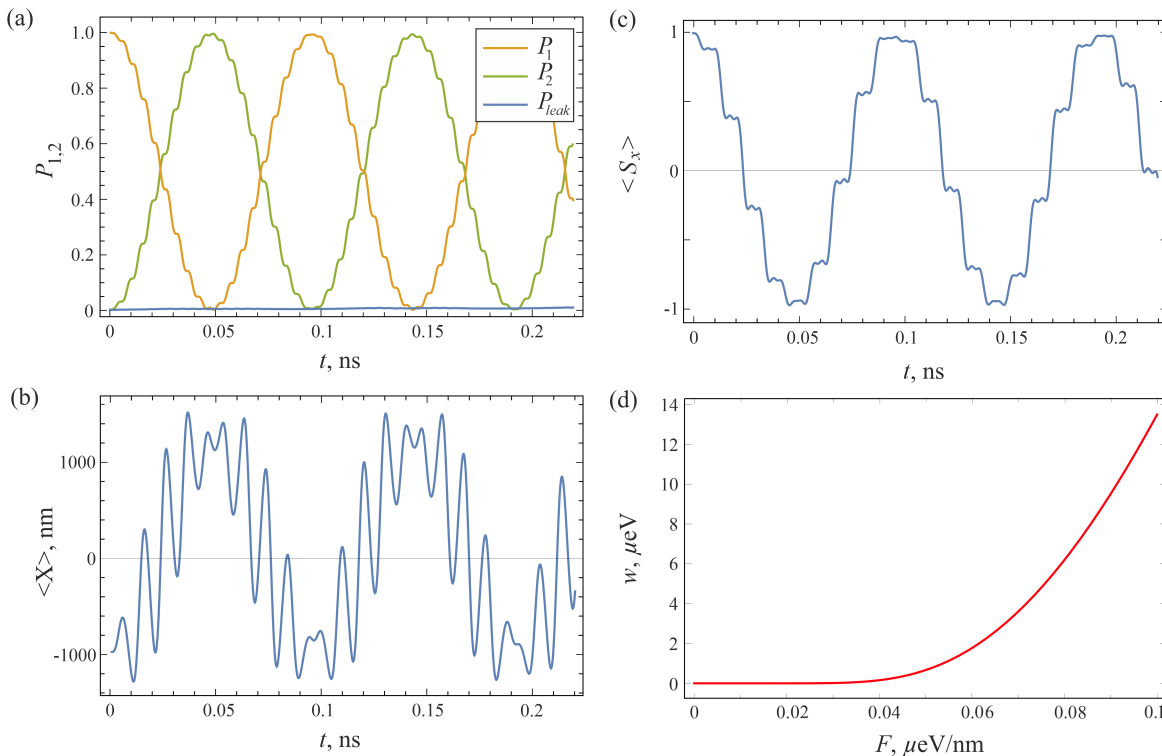


FIG. 7. Dynamics for the field amplitude $F = 0.05 \mu\text{eV/nm}$, analogous to Fig. 6. (a) Populations $P_{1,2}(t) = |C_{1,2}(t)|^2$ and leakage $P_{leak} = 1 - |C_1|^2 - |C_2|^2$. The linear frequency of Rabi oscillations is $f_R = 20$ GHz, and the leakage remains below 1%. (b,c) Time evolution of the expectation values $\langle X(t) \rangle$ and $\langle S_x(t) \rangle$. (d) Estimate (29) for the leakage rate into the continuum as a function of F . When the field amplitude is reduced from 0.1 to $0.05 \mu\text{eV/nm}$, the leakage rate decreases by more than one order of magnitude.

shown by the lower curve in Fig. 7(a), is substantially smaller than for $F = 0.1 \mu\text{eV/nm}$ and remains below one percent over the considered time interval.

This strong suppression of leakage is related to the exponential dependence of the ionization rate $w(F)$ on the electric-field amplitude. In the simplest case of a potential well with a single discrete level, the ionization rate in energy units can be estimated as [49]

$$w(F) \approx 2|E_1| \left(\frac{3F}{\pi F_0} \right)^{1/2} \exp\left(-\frac{2F_0}{3F} \right), \quad (29)$$

where $|E_1|$ is the absolute value of the discrete-level energy from which ionization occurs and F_0 characterizes the effective barrier field. In the present system it can be estimated as

$$F_0 = \frac{\Delta_B - |E_1|}{L}. \quad (30)$$

The estimate (30) gives $F_0 \sim 0.4 \mu\text{eV/nm}$. The resulting dependence (29) is shown in Fig. 7(d). For $F = 0.1 \mu\text{eV/nm}$, it yields an ionization rate of order $w \sim 6 \mu\text{eV}$, corresponding to the leakage time $\tau \sim \hbar/w \sim 0.1$ ns. This estimate is consistent with the appearance of appreciable leakage in Fig. 6(a). When the field is reduced to $F = 0.05 \mu\text{eV/nm}$, the leakage

rate decreases to approximately $w \sim 0.4 \mu\text{eV}$, and the corresponding leakage time becomes much longer than the characteristic Rabi period. As a result, the leakage is barely visible in Fig. 7(a).

The estimate (30) gives $F_0 \sim 0.4 \mu\text{eV/nm}$. The resulting dependence (29) is shown in Fig. 7(d). For $F = 0.1 \mu\text{eV/nm}$, it yields an ionization rate of order $w \sim 12 \mu\text{eV}$, corresponding to the leakage time $\tau \sim \hbar/w \sim 0.05$ ns. This estimate is consistent with the appearance of appreciable leakage in Fig. 6(a). When the field is reduced to $F = 0.05 \mu\text{eV/nm}$, the leakage rate decreases to approximately $w \sim 0.8 \mu\text{eV}$, and the corresponding leakage time becomes much longer than the characteristic Rabi period. As a result, the leakage is barely visible in Fig. 7(a).

The comparison of Figs. 6 and 7 therefore identifies the physically relevant operating regime of the double-kink system. The continuum does not preclude coherent two-level dynamics, but it imposes an upper bound on the useful driving amplitude. Within this bound, the Rabi frequency remains in the tens-of-GHz range, while the leakage probability can be reduced to a level that is small on the time scale of several Rabi periods. Thus, the double-kink geometry realizes a lithographically defined two-level subsystem whose coherent dynamics can be driven electrically and whose coupling to continuum

edge states can be quantified within the same model. This provides the basis for the conclusions summarized in the next section.

V. RESULTS AND CONCLUSIONS

We have studied localized and continuum states at the 1D edge of a HgTe/CdHgTe QW with two lithographically defined kinks. In a static in-plane magnetic field, the helical edge spectrum acquires a gap, and changes in the edge orientation modify the magnetic-field-induced edge mass. We have shown that, for suitable geometric parameters and magnetic-field direction, this produces two localized in-gap states at the kinks. These states form a lithographically defined two-level subsystem whose parameters are controlled by the edge shape, the kink separation, and the orientation of the magnetic field.

The main result of the work is that this two-level subsystem can undergo coherent electrically driven Rabi oscillations even when continuum edge states are included explicitly. For the parameters considered, the linear Rabi frequency reaches 20–40 GHz. The continuum states do not destroy the two-level dynamics, but they pro-

vide a leakage channel that constrains the useful range of driving amplitudes. Stronger electric fields increase the Rabi frequency but enhance population leakage, whereas weaker fields suppress leakage while preserving GHz-scale coherent oscillations. This trade-off defines an operating regime in which fast electric manipulation remains compatible with a well-preserved two-level dynamics.

The present analysis establishes a direct link between magnetic-field-induced corner-state physics and driven coherent dynamics of localized edge-state excitations. It also shows that the double-kink geometry provides more than a static pair of in-gap levels: it offers a controlled setting in which resonant transfer, electric-dipole coupling, and continuum-induced leakage can be analyzed within a single effective edge-state framework.

ACKNOWLEDGMENTS

D.V.K and D.P.K. are supported by the State Assignment of the Ministry of Science and Higher Education of the Russian Federation, project No. FSWR-2026-0004. S.S.K. and F.T. acknowledge financial support from the French Agence Nationale pour la Recherche through the “Cantor” project, Grant No. ANR-23-CE24-0022, and the “Teaser” project, Grant No. ANR-24-CE24-4830.

-
- [1] M. Z. Hasan and C. L. Kane, Colloquium: Topological insulators, *Rev. Mod. Phys.* **82**, 3045 (2010).
 - [2] X.-L. Qi and S.-C. Zhang, Topological insulators and superconductors, *Rev. Mod. Phys.* **83**, 1057 (2011).
 - [3] B. A. Bernevig, T. L. Hughes, and S.-C. Zhang, Quantum spin hall effect and topological phase transition in hgte quantum wells, *Science* **314**, 1757 (2006).
 - [4] M. König, S. Wiedmann, C. Brüne, A. Roth, H. Buhmann, L. W. Molenkamp, X.-L. Qi, and S.-C. Zhang, Quantum spin hall insulator state in hgte quantum wells, *Science* **318**, 766 (2007).
 - [5] S. Wu, V. Fatemi, Q. D. Gibson, K. Watanabe, T. Taniguchi, R. J. Cava, and P. Jarillo-Herrero, Observation of the quantum spin hall effect up to 100 kelvin in a monolayer crystal, *Science* **359**, 76 (2018).
 - [6] S. S. Krishtopenko and F. Teppe, Quantum spin hall insulator with a large bandgap, dirac fermions, and bilayer graphene analog, *Sci. Adv.* **4**, eaap7529 (2018).
 - [7] M. Meyer, J. Baumbach, S. Krishtopenko, A. Wolf, M. Emmerling, S. Schmid, M. Kamp, B. Jouault, J.-B. Rodriguez, E. Tournie, T. Müller, R. Thomale, G. Bastard, F. Teppe, F. Hartmann, and S. Höfling, Quantum spin hall effect in iii-v semiconductors at elevated temperatures: Advancing topological electronics, *Sci. Adv.* **11**, eadz2408 (2025).
 - [8] W. A. Benalcazar, B. A. Bernevig, and T. L. Hughes, Quantized electric multipole insulators, *Science* **357**, 61 (2017).
 - [9] W. A. Benalcazar, B. A. Bernevig, and T. L. Hughes, Electric multipole moments, topological multipole moment pumping, and chiral hinge states in crystalline insulators, *Phys. Rev. B* **96**, 245115 (2017).
 - [10] J. Langbehn, Y. Peng, L. Trifunovic, F. von Oppen, and P. W. Brouwer, Reflection-symmetric second-order topological insulators and superconductors, *Phys. Rev. Lett.* **119**, 246401 (2017).
 - [11] F. Schindler, A. M. Cook, M. G. Vergniory, Z. Wang, S. S. P. Parkin, B. A. Bernevig, and T. Neupert, Higher-order topological insulators, *Sci. Adv.* **4**, eaat0346 (2018).
 - [12] F. Schindler, Z. Wang, M. G. Vergniory, A. M. Cook, A. Murani, S. Sengupta, A. Yu., Kasumov, R. Deblock, S. Jeon, I. Drozdov, H. Bouchiat, S. Guéron, A. Yazdani, B. A. Bernevig, and T. Neupert, Higher-order topology in bismuth, *Nat. Phys.* **15**, 918 (2018).
 - [13] B. Xie, H.-X. Wang, X. Zhang, P. Zhan, J.-H. Jiang, M. Lu, and Y. Chen, Higher-order band topology, *Nat. Rev. Phys.* **3**, 520 (2021).
 - [14] M. Serra-Garcia, V. Peri, R. Süsstrunk, O. R. Bilal, T. Larsen, L. G. Villanueva, and S. D. Huber, Observation of a phononic quadrupole topological insulator, *Nature* **555**, 342 (2018).
 - [15] C. W. Peterson, W. A. Benalcazar, T. L. Hughes, and G. Bahl, A quantized microwave quadrupole insulator with topologically protected corner states, *Nature* **555**, 346 (2018).
 - [16] X.-D. Chen, W.-M. Deng, F.-L. Shi, F.-L. Zhao, M. Chen, and J.-W. Dong, Direct observation of corner states in second-order topological photonic crystal slabs, *Phys. Rev. Lett.* **122**, 233902 (2019).
 - [17] S. S. Krishtopenko, W. Knap, and F. Teppe, Phase transitions in two tunnel-coupled hgte quantum wells: Bilayer graphene analogy and beyond, *Sci. Rep.* **6**, 30755 (2016).

- [18] L. S. Bovkun, A. V. Ikonnikov, V. Y. Aleshkin, K. V. Maremyanin, N. N. Mikhailov, S. A. Dvoretiskii, S. S. Krishtopenko, F. Teppe, B. A. Piot, M. Potemski, M. Orlita, and V. I. Gavrilenko, Magnetospectroscopy of double hgte/cdhgte qws with inverted band structure in high magnetic fields up to 30 t, *Opto-electron. Rev.* **27**, 213 (2019).
- [19] A. V. Ikonnikov, S. S. Krishtopenko, L. S. Bovkun, N. N. Mikhailov, S. A. Dvoretiskii, B. A. Piot, M. Potemski, M. Orlita, F. Teppe, and V. I. Gavrilenko, Origin of structure inversion asymmetry in double hgte quantum wells, *JETP Lett.* **116**, 547 (2022).
- [20] L. S. Bovkun, S. S. Krishtopenko, V. Y. Aleshkin, N. N. Mikhailov, S. A. Dvoretiskii, F. Teppe, M. Orlita, V. I. Gavrilenko, and A. V. Ikonnikov, Simultaneous observation of the cyclotron resonances of electrons and holes in a hgte/cdhgte double quantum well under “optical gate” effect, *JETP Lett.* **118**, 867 (2023).
- [21] S. S. Krishtopenko, A. V. Ikonnikov, B. Jouault, and F. Teppe, Disorder-induced phase transitions in double hgte quantum wells, *Phys. Rev. B* **111**, 045431 (2025).
- [22] S. Ruffenach, S. S. Krishtopenko, L. S. Bovkun, A. V. Ikonnikov, M. Marcinkiewicz, C. Consejo, M. Potemski, B. Piot, M. Orlita, B. R. Semyagin, M. A. Putyato, E. A. Emelyanov, V. V. Preobrazhenskii, W. Knap, F. Gonzalez-Posada, G. Boissier, E. Tournié, F. Teppe, and V. I. Gavrilenko, Magnetoabsorption of Dirac fermions in gapless three-layer InAs/GaSb/InAs quantum wells, *JETP Lett.* **106**, 727 (2017).
- [23] S. S. Krishtopenko, S. Ruffenach, F. Gonzalez-Posada, G. Boissier, M. Marcinkiewicz, M. A. Fadeev, A. M. Kadykov, V. V. Rumyantsev, S. V. Morozov, V. I. Gavrilenko, C. Consejo, W. Desrat, B. Jouault, W. Knap, E. Tournié, and F. Teppe, Temperature-dependent terahertz spectroscopy of inverted-band three-layer inas/gasb/inas quantum well, *Phys. Rev. B* **97**, 245419 (2018).
- [24] S. S. Krishtopenko, S. Ruffenach, F. Gonzalez-Posada, C. Consejo, W. Desrat, B. Jouault, W. Knap, M. A. Fadeev, A. M. Kadykov, V. V. Rumyantsev, S. V. Morozov, G. Boissier, E. Tournié, V. I. Gavrilenko, and F. Teppe, Terahertz spectroscopy of two-dimensional semimetal in three-layer InAs/GaSb/InAs quantum well, *JETP Lett.* **109**, 96 (2019).
- [25] S. S. Krishtopenko, W. Desrat, K. E. Spirin, C. Consejo, S. Ruffenach, F. Gonzalez-Posada, B. Jouault, W. Knap, K. V. Maremyanin, V. I. Gavrilenko, G. Boissier, J. Torres, M. Zaknoute, E. Tournié, and F. Teppe, Massless dirac fermions in iii-v semiconductor quantum wells, *Phys. Rev. B* **99**, 121405(R) (2019).
- [26] C. Avogadri, S. Gebert, S. S. Krishtopenko, I. Castillo, C. Consejo, S. Ruffenach, C. Roblin, C. Bray, Y. Krupko, S. Juillaguet, S. Contreras, A. Wolf, F. Hartmann, S. Höfling, G. Boissier, J.-B. Rodriguez, S. Nanot, E. Tournié, F. Teppe, and B. Jouault, Large inverted band gap in strained three-layer inas/gasb quantum wells, *Phys. Rev. Research* **4**, L042042 (2022).
- [27] S. S. Krishtopenko, Higher-order topological insulator in cubic semiconductor quantum wells, *Sci. Rep.* **11**, 21060 (2021).
- [28] M. Ezawa, Topological switch between second-order topological insulators and topological crystalline insulators, *Phys. Rev. Lett.* **121**, 116801 (2018).
- [29] Y. Ren, Z. Qiao, and Q. Niu, Engineering corner states from two-dimensional topological insulators, *Phys. Rev. Lett.* **124**, 166804 (2020).
- [30] C. Chen, Z. Song, J.-Z. Zhao, Z. Chen, Z.-M. Yu, X.-L. Sheng, and S. A. Yang, Universal approach to magnetic second-order topological insulator, *Phys. Rev. Lett.* **125**, 056402 (2020).
- [31] S. S. Krishtopenko and F. Teppe, Magnetic field induced corner states in quantum spin hall insulators, *Phys. Rev. B* (2026), accepted, ArXiv:2303.09260.
- [32] S. S. Krishtopenko, M. Antezza, and F. Teppe, Disorder-induced phase transition in dirac systems beyond the linear approximation, *Phys. Rev. B* **101**, 205424 (2020).
- [33] S. S. Krishtopenko, M. Antezza, and F. Teppe, Disorder-induced topological phase transition in hgcdte crystals, *Phys. Rev. B* **106**, 115203 (2022).
- [34] S. S. Krishtopenko, A. V. Ikonnikov, F. Hartmann, S. Höfling, B. Jouault, and F. Teppe, Quasiparticle picture of topological phase transitions induced by interactions, *Phys. Rev. Research* **7**, 033116 (2025).
- [35] D. V. Khomitsky, K. S. Kabaev, and E. A. Lavrukina, Spin resonance in a quantum dot at the edge of a topological insulator with the inclusion of continuum states, *J. Exp. Theor. Phys.* **131**, 809 (2020).
- [36] D. V. Khomitsky and E. A. Lavrukina, *J. Exp. Theor. Phys.* (2026), accepted.
- [37] R. A. Niyazov, D. N. Aristov, and V. Y. Kachorovskii, Effective hamiltonian of topologically protected qubit in a helical crystal, *JETP Lett.* **118**, 376 (2023).
- [38] M. König, H. Buhmann, L. W. Molenkamp, T. Hughes, C.-X. Liu, X.-L. Qi, and S.-C. Zhang, The quantum spin hall effect: Theory and experiment, *J. Phys. Soc. Jpn.* **77**, 031007 (2008).
- [39] M. V. Durnev and S. A. Tarasenko, Magnetic field effects on edge and bulk states in topological insulators based on hgte/cdhgte quantum wells with strong natural interface inversion asymmetry, *Phys. Rev. B* **93**, 075434 (2016).
- [40] S. S. Krishtopenko, A. M. Kadykov, S. Gebert, S. Ruffenach, C. Consejo, J. Torres, C. Avogadri, B. Jouault, W. Knap, N. N. Mikhailov, S. A. Dvoretiskii, and F. Teppe, Many-particle effects in optical transitions from zero-mode landau levels in hgte quantum wells, *Phys. Rev. B* **102**, 041404(R) (2020).
- [41] S. Ruffenach, S. S. Krishtopenko, A. V. Ikonnikov, C. Consejo, J. Torres, X. Baudry, P. Ballet, B. Jouault, and F. Teppe, Many-particle hybridization of optical transitions from zero-mode landau levels in hgte quantum wells, *Phys. Rev. B* **113**, L161108 (2026).
- [42] R. Winkler, *Spin-Orbit Coupling Effects in Two-Dimensional Electron and Hole Systems* (Springer, New York, 2003).
- [43] S. S. Krishtopenko and F. Teppe, Realistic picture of helical edge states in hgte quantum wells, *Phys. Rev. B* **97**, 165408 (2018).
- [44] D. V. Khomitsky, E. A. Lavrukina, and E. Y. Sherman, Electric dipole spin resonance at shallow donors in quantum wires, *Phys. Rev. B* **99**, 014308 (2019).
- [45] D. Khomitsky, E. Lavrukina, and E. Sherman, Spin rotation by resonant electric field in few-level quantum dots: Floquet dynamics and tunneling, *Phys. Rev. Applied* **14**, 014090 (2020).
- [46] G. M. Minkov, A. V. Germanenko, O. E. Rut, A. A. Sherstobitov, S. A. Dvoretiskii, and N. N. Mikhailov, Weak antilocalization in hgte quantum wells with inverted energy spectra, *Phys. Rev. B* **85**, 235312 (2012).

- [47] A. M. Kadykov, S. S. Krishtopenko, B. Jouault, W. Desrat, W. Knap, S. Ruffenach, C. Consejo, J. Torres, S. V. Morozov, N. N. Mikhailov, S. A. Dvoretiskii, and F. Teppe, Temperature-induced topological phase transition in hgte quantum wells, *Phys. Rev. Lett.* **120**, 086401 (2018).
- [48] D. V. Khomitsky, E. A. Lavrukina, A. V. Telezhnikov, and M. S. Zholudev, Modeling of landau levels, hall and longitudinal resistance in the topological anderson insulator based on hgte/hg_{0.3}cd_{0.7}te quantum well, *Fizika i Tekhnika Poluprovodnikov* **59**, 337 (2025).
- [49] A. M. Perelomov, V. S. Popov, and M. V. Terent'ev, Ionization of atoms in an alternating electric field, *JETP* **23**, 924 (1966).